Numerical computations of faceted pattern formation in snow crystal growth

John W. Barrett
Department of Mathematics, Imperial College London, London SW7 2AZ, United Kingdom

Harald Garcke*
Fakultät für Mathematik, Universität Regensburg, 93040 Regensburg, Germany

Robert Nürnberg
Department of Mathematics, Imperial College London, London SW7 2AZ, United Kingdom

(Received 19 April 2012; published 26 July 2012)

Faceted growth of snow crystals leads to a rich diversity of forms with remarkable sixfold symmetry. Snow crystal structures result from diffusion-limited crystal growth in the presence of anisotropic surface energy and anisotropic attachment kinetics. It is by now well understood that the morphological stability of ice crystals strongly depends on supersaturation, crystal size, and temperature. Until very recently it was very difficult to perform numerical simulations of this highly anisotropic crystal growth. In particular, obtaining facet growth in combination with dendritic branching is a challenging task. We present numerical simulations of snow crystal growth in two and three spacial dimensions using a computational method recently introduced by the present authors. We present both qualitative and quantitative computations. In particular, a linear relationship between tip velocity and supersaturation is observed. In our computations, surface energy effects, although small, have a pronounced effect on crystal growth. We compute solid plates, solid prisms, hollow columns, needles, dendrites, capped columns, and scrolls on plates. Although all these forms appear in nature, it is a significant challenge to reproduce them with the help of numerical simulations for a continuum model.

DOI: 10.1103/PhysRevE.86.011604 PACS number(s): 81.10.Aj, 07.05.Tp, 81.30.Fb

I. INTRODUCTION

Snow crystals grown from a supersaturated vapor lead to a variety of complex and often very symmetric patterns. Crystallization from vapor is a fundamental phase transition, and good understanding of it is crucial for many applications. Numerous experiments have been performed, and compilations of photographs of artificial and natural snowflakes reveal their beauty and complexity; see [1] and the review [2]. The precise forms of snow crystals depend in a very subtle way on temperature and supersaturation. Nakaya [1] analyzed these dependencies in detail and combined his observations in his by now famous Nakaya snow crystal morphology diagram; see Fig. 1. At temperatures just below the freezing temperature, thick plates grow at lower supersaturations and platelike dendritic forms appear at higher supersaturations. At temperatures around $-5\,^{\circ}$C, solid prisms grow at lower supersaturations and hollow columns and needlelike crystals grow at higher supersaturations. If the temperature is decreased below $-10\,^{\circ}$C, one observes thin solid plates at low supersaturations, whereas dendrites form at high supersaturations. Below $-25\,^{\circ}$C, again columns form at high supersaturations. The results from Nakaya [1], which led to the snow crystal morphology diagram, have been confirmed by many subsequent experimental studies. Although the experiments give a clear picture, the physics behind the snow crystal morphology diagram are not yet understood.

A continuum mathematical modeling of snow crystal growth leads to a quasistatic diffusion problem for the diffusion of the vapor molecules. The diffusion equation has to be solved together with rather complex boundary conditions on the free boundary between vapor and solid. The conditions on this interface are given by the continuity equation relating the flux of vapor molecules onto the interface to the interface velocity and an equation describing the attachment kinetics, taking surface energy effects into account. In the latter condition, which is a modified Gibbs-Thomson law, the hexagonal anisotropy of snow crystals also is a factor. Altogether, a highly nonlinear free boundary problem is obtained.

Many of the parameters in snow crystal growth models are not known with sufficient precision. In particular, the surface energy density as a function of orientation is not known in detail. A similar statement applies to the condensation coefficient, which embodies the attachment kinetics of how water molecules are incorporated into the ice lattice. For example, it is not known how the condensation coefficient depends on the crystal orientation; see [2] and the references therein for details. Let us discuss the difficulties arising in this context in more detail. The surface structure of ice is quite complicated, and phenomena like surface roughening, surface melting, and kinetic roughening can occur; see, for example, [2,4]. In particular, whether and how these phenomena occur depend on the temperature and on the growth velocity. It is understood that while at low temperatures the equilibrium structure is close to a flat, faceted surface, above a roughening temperature the crystal becomes completely rough, and just below the melting temperature a quasiliquid layer forms on the solid surface. It is frequently argued that surface melting can be viewed as a more developed form of surface roughening. For further information on surface roughening and surface melting, we refer readers to [2,4–8]. Finally, let us mention that in [2, §2.6] it is discussed how the surface structure and, in particular, how surface roughening and kinetic roughening

*harald.garcke@mathematik.uni-regensburg.de

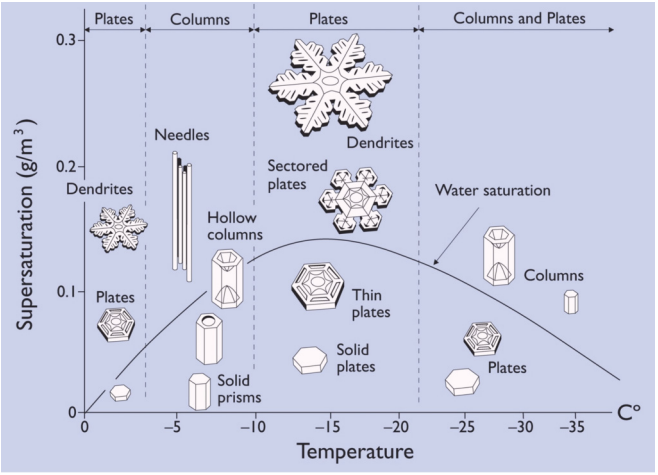

FIG. 1. (Color online) The Nakaya diagram illustrates which snow crystal forms appear at different temperatures and supersaturations. This figure is taken from [3]; see also [2].

may affect the condensation coefficient in the Gibbs-Thomson law, although a precise qualitative description of their influence remains an open problem. Hence in this paper, for simplicity, we assume that the attachment coefficient only depends on the local orientation of the growing crystal. Nevertheless, we demonstrate that computations for this basic continuum model manage to produce many realistic snow crystal shapes.

Because it is highly nonlinear and geometrically very involved, the complete free boundary problem is difficult to analyze theoretically. However, there exists a large body of literature on numerical computations for diffusion-limited growth and the formation of dendrites, which we now briefly discuss.

Numerical approaches for crystal growth based on a continuum description usually employ either sharp interface models, in which the solidification front is tracked explicitly, or phase field models, in which the solidification front is modeled by a thin diffusional layer. In sharp interface approaches the front is described with the help of a parametrization (see [9–14]) or by using a level set function (see [15]). In a phase field method, a new order parameter—the phase field—is introduced, which at the interface rapidly changes its value between two fixed values that describe the different phases; see [16–20]. A popular discrete model for the simulation of crystal growth is cellular automata; see [21–23]. We refer in particular to the pioneering work of Gravner and Griffeath [23], who were able to compute three-dimensional evolving patterns which resemble growing snow crystals. Moreover, molecular dynamics simulations are used to understand the surface structure and the growth

TABLE I. Values of $u_{\partial\Omega} = c_{\text{super}}/c_{\text{sat}}$ depending on T and ϱ_{super}.

	Supersaturation ϱ_{super} (g/m^3)					
T (°C)	0.01	0.02	0.05	0.1	0.2	0.3
−1	0.002	0.005	0.011	0.023	0.048	0.069
−2	0.003	0.005	0.012	0.025	0.049	0.074
−5	0.003	0.006	0.016	0.031	0.063	0.094
−10	0.005	0.010	0.024	0.048	0.095	0.143
−15	0.007	0.015	0.037	0.074	0.147	0.221
−30	0.030	0.060	0.150	0.300	0.601	0.901

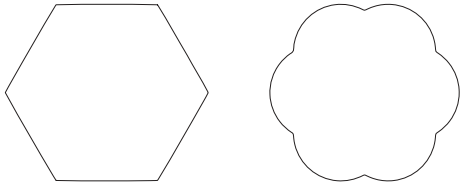

FIG. 2. Scaled Wulff shape (left) and polar plot (right) in $\mathbb{R}^2$ for Eq. (12) with $\epsilon = 0.01$ and $\theta_0 = 0$.

kinetics of ice [24–26]. Although many computations have been performed, a quantitative numerical description of facet growth in combination with dendritic branching is missing.

In recent research a new parametric approach for interface motion has been developed [27,28]. In this method the mesh quality of the interface approximation, which is given by a polyhedral surface mesh, does not deteriorate during the evolution—most earlier approaches had to deal with mesh degeneracies, for example, by remeshing the interface approximation. In addition, the present authors were able to include anisotropy effects into curvature-driven hypersurface evolution in a numerically stable way. This allows the method to compute in situations in which the anisotropy is faceted; see [14,29–31]. We remark that extending the ideas from [29,30] on the stable approximation of faceted interface growth to a phase field approach forms part of the authors' current research [32].

It is the goal of this paper to demonstrate that with the numerical method introduced in Refs. [14,27,28,30] it is possible to compute a significant number of different types of snow crystals, such as solid plates, solid prisms, hollow columns, needles, dendrites, capped columns, and scrolls on plates.

In our numerical computations the anisotropy in the surface energy density has a large impact on the resulting morphologies. Of course, numerical simulations alone cannot decide whether surface energy effects are important in order to obtain patterns in snow crystal growth, but a comparison of numerical computations with experiments might help us understand this issue better. In addition, it might be possible to obtain more precise estimates for the size of the condensation coefficient as a function of orientation. In particular, there is the possibility that the condensation coefficient depends on the supersaturation (see, for example, [33]) and the implication of this fact on pattern formation in crystal growth will be considered in future research.

We also present some quantitative results, which first of all show the relative sizes of the quantities entering the surface

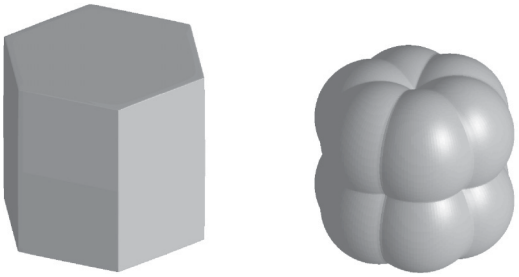

FIG. 3. Scaled Wulff shape (left) and polar plot (right) in $\mathbb{R}^3$ for Eq. (13) with $\epsilon = 0.01$.

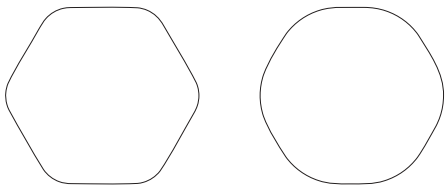

FIG. 4. Scaled Wulff shape in $\mathbb{R}^2$ for Eq. (15) with $\sigma = 1$ (left) and $\sigma = 5$ (right) with $\epsilon = 0.01$.

attachment kinetics. In addition, we show that the tip velocity for a dendrite growing into a supersaturated vapor depends linearly on the supersaturation. This linear relationship has been already observed in experiments for growing needles (see [34]), and our computations might help to relate parameters in the theoretical model to experiments.

II. A CONTINUUM MODEL FOR SNOW CRYSTAL GROWTH

We consider a continuum model for snow crystal growth, which consists of an ice crystal growing from water vapor, as discussed, for example, in Refs. [2,35], and nondimensionalize it. Let c denote the water vapor number density in the gas phase. The diffusion equation in the gas phase (see [2, Eq. (2)]) is then

$$c_t - \mathcal{D}\,\Delta\, c = 0 \quad \text{in} \quad \Omega_+(t), \tag{1}$$

where $\Omega_+(t)$ is the domain occupied by the gas phase and $\mathcal{D}$ is the corresponding diffusion constant. The mass balance at the gas-solid interface $\Gamma(t)$ gives rise to

$$\mathcal{D}\,\frac{\partial c}{\partial \vec{\nu}} = (c_{\text{solid}} - c)\,\mathcal{V} \quad \text{on} \quad \Gamma(t), \tag{2}$$

where $c_{\text{solid}} \approx 3 \times 10^{28}\,\text{m}^{-3}$ is the number density for ice. In addition, $\vec{\nu}$ is the unit normal to $\Gamma(t)$ pointing into $\Omega_+(t)$ and $\mathcal{V}$ is the velocity of $\Gamma(t)$ in the direction $\vec{\nu}$. In Ref. [2, Eq. (3)] the term $c\,\mathcal{V}$ is neglected since $c \ll c_{\text{solid}}$. Furthermore, taking surface tension effects and attachment kinetics into account, we require (cf. [2, Eq. (23)])

$$c = c_{\text{sat}}\left(1 - \delta\,\kappa_\gamma + \frac{\mathcal{V}}{\beta(\vec{\nu})\,v_{\text{kin}}}\right) \quad \text{on} \quad \Gamma(t)\,.$$

Here v_{kin} is the kinetic velocity, $\delta = \hat{\gamma}/(c_{\text{solid}}\,K\,T) \approx 1\,\text{nm} = 10^{-3}\ \mu\text{m}$, where $\hat{\gamma} \approx 0.1\,\text{Jm}^{-2}$ represents the typical order of the surface tension of ice, $K \approx 1.4 \times 10^{-23}\,\text{JK}^{-1}$ is the Boltzmann constant, T is the temperature, and $c_{\text{sat}} = c_{\text{sat}}(T)$ is the equilibrium number density above a flat ice surface, which is dependent on temperature. In addition, κ_γ is the anisotropic mean curvature which incorporates the hexagonal anisotropy of the surface energy density. Moreover, β is the condensation coefficient, denoted by α in Ref. [2], which depends on the orientation of the crystal via the normal $\vec{\nu}$. Finally, we complement (1) with the boundary condition

$$c = c_\infty \quad \text{on} \quad \partial\Omega = \partial\Omega_+(t) \setminus \Gamma(t), \tag{3}$$

where $c_\infty := c_{\text{sat}} + c_{\text{super}}$ describes the water vapor number density far away from the interface. Here, for convenience, we choose a domain $\Omega \subset \mathbb{R}^d$, $d = 2,3$, with $\Omega_+(t) \subset \Omega$, that is large enough so that boundary effects can be neglected. Moreover, c_{super} is related to the supersaturation ϱ_{super} by

$$\varrho_{\text{super}} = \text{m}_{\text{H}_2\text{O}}\,c_{\text{super}}, \tag{4}$$

with $\text{m}_{\text{H}_2\text{O}} \approx 3 \times 10^{-23}\,\text{g}$ denoting the mass of a water molecule. We recall that the supersaturation ϱ_{super} appears on the vertical axis in Fig. 1.

It remains to introduce the anisotropic mean curvature κ_γ. Instead of a constant surface energy density, we choose γ to be dependent on the orientation of the interface. The effect of the underlying crystal structure is encoded into the surface energy by allowing $\gamma = \gamma(\vec{\nu})$, where as stated above $\vec{\nu}$ is the unit normal to the solid boundary $\Gamma(t)$ pointing into the vapor region $\Omega_+(t)$. The total surface energy of an interface Γ, scaled by the typical order $\hat{\gamma} \approx 0.1\,\text{Jm}^{-2}$, is now given by the surface integral

$$\int_\Gamma \gamma(\vec{\nu})ds.$$

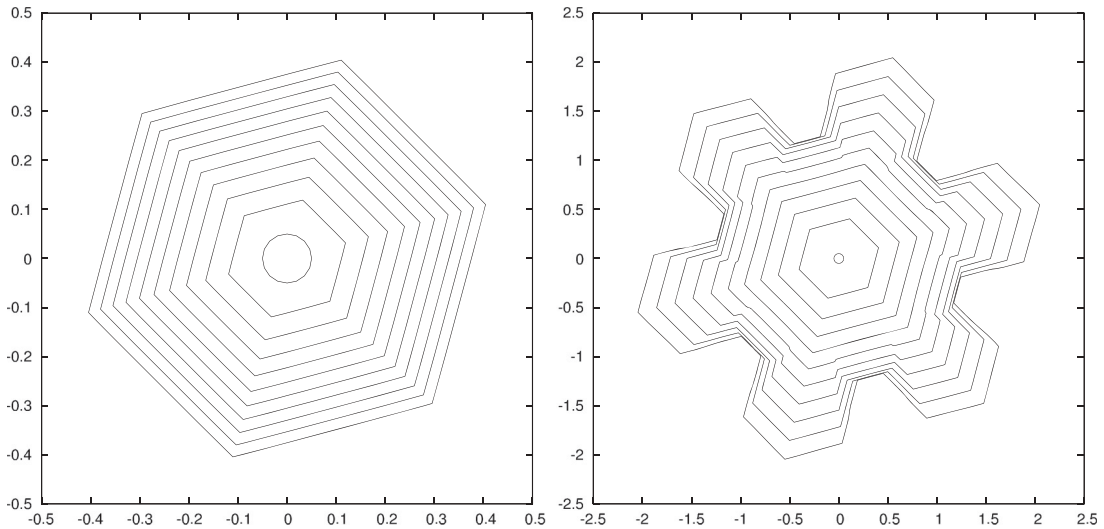

FIG. 5. [$\Omega = (-4,4)^2$, $u_{\partial\Omega} = 0.004$, $\gamma = \beta = \gamma_{\text{hex}}$] $\Gamma^h(t)$ for $t = 0, 5, \ldots, 50$ (left) and for $t = 0, 50, \ldots, 500$ (right). Parameters are $N_f = 256$, $N_c = 4$, $K_\Gamma^0 = 16$, and $\tau = 0.1$.

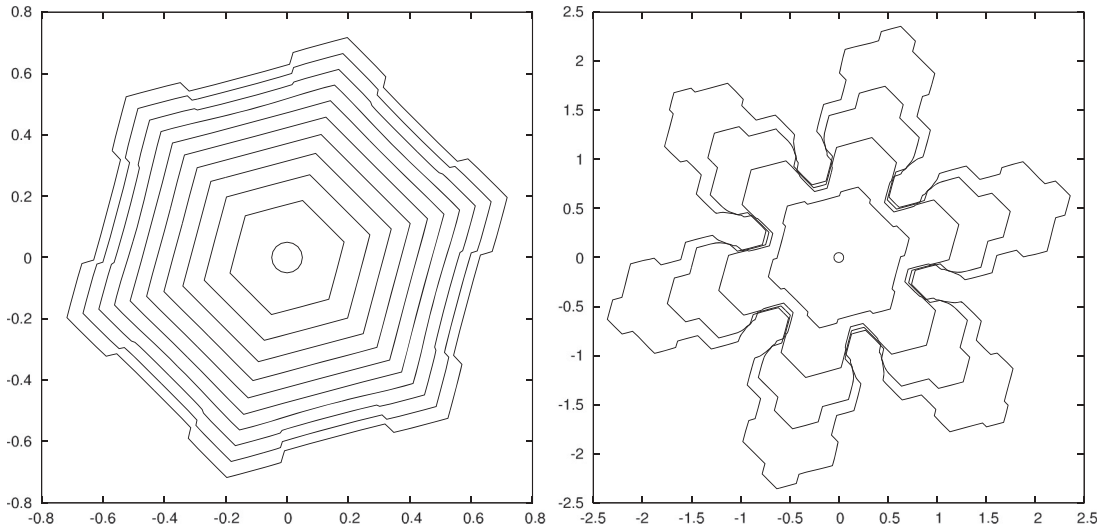

FIG. 6. $[\Omega = (-4,4)^2,\ u_{\partial\Omega} = 0.01,\ \gamma = \beta = \gamma_{\text{hex}}]$ $\Gamma^h(t)$ for $t = 0, 5, \ldots, 50$ (left), and for $t = 0, 50, \ldots, 200$ (right). Parameters are $N_f = 512$, $N_c = K_\Gamma^0 = 16$, and $\tau = 5 \times 10^{-3}$.

It is convenient to extend γ to be a positively homogeneous function of degree 1; that is, we define $\tilde{\gamma}(\vec{p}) = |\vec{p}|\,\gamma(\vec{p}/|\vec{p}|)$ for all $\vec{p} \neq \vec{0}$ and refer to $\tilde{\gamma}$ as γ from now on. The first variation of the above energy can now be computed as

$$\kappa_\gamma := -\nabla_s \cdot \gamma'(\vec{\nu}),$$

that is, $\frac{d}{dt}\int_{\Gamma(t)} \gamma(\vec{\nu})ds = -\int_{\Gamma(t)} \kappa_\gamma\, \mathcal{V} ds$, where $\nabla_s \cdot$ is the tangential divergence on Γ and γ' is the gradient of γ (see, e.g., [36–38] and also [14,30]).

We now nondimensionalize the problem. As a length scale we choose R, which we set to be 100 μm. As a time scale we choose

$$\tilde{t} = \frac{R^2}{\mathcal{D}}\,\frac{c_{\text{solid}}}{c_{\text{sat}}}.$$

In addition, we nondimensionalize the concentration by introducing

$$u = \frac{c - c_{\text{sat}}}{c_{\text{sat}}}. \tag{5}$$

Then, in terms of the new independent variables $\hat{\vec{x}} = \vec{x}/R$ and $\hat{t} = t/\tilde{t}$, we obtain (on dropping the $\hat{}$ notation for the new variables for ease of exposition) the equations

$$\frac{c_{\text{sat}}}{c_{\text{solid}}}\,\partial_t u - \Delta u = 0 \quad \text{in } \Omega_+(t),$$

$$\frac{\partial u}{\partial \vec{\nu}} = \mathcal{V} \quad \text{on } \Gamma(t), \tag{6}$$

$$\frac{\rho\,\mathcal{V}}{\beta(\vec{\nu})} = \alpha\,\kappa_\gamma + u \quad \text{on } \Gamma(t), \tag{7}$$

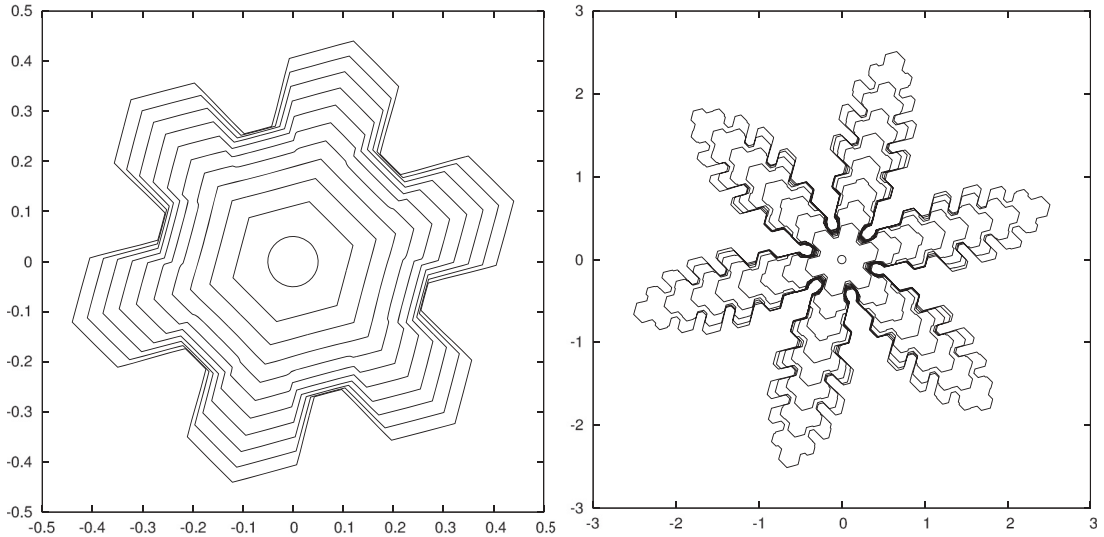

FIG. 7. $[\Omega = (-4,4)^2,\ u_{\partial\Omega} = 0.04,\ \gamma = \beta = \gamma_{\text{hex}}]$ $\Gamma^h(t)$ for $t = 0, 0.5, \ldots, 5$ (left), and for $t = 0, 5, \ldots, 40$ (right). Parameters are $N_f = 1024$, $N_c = K_\Gamma^0 = 64$ and $\tau = 2.5 \times 10^{-3}$.

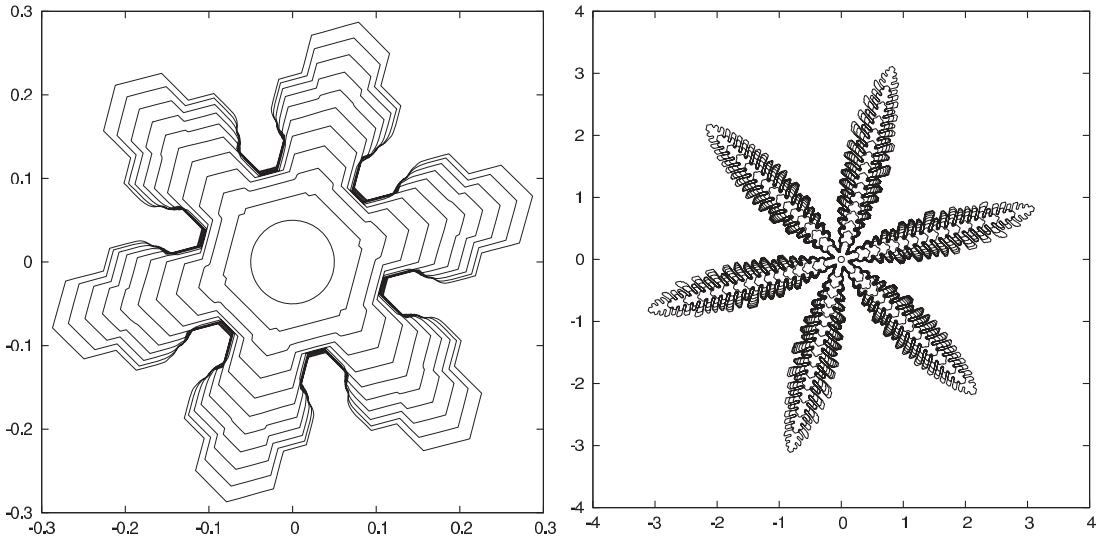

FIG. 8. [$\Omega = (-4,4)^2$, $u_{\partial\Omega} = 0.2$, $\gamma = \beta = \gamma_{\text{hex}}$] $\Gamma^h(t)$ for $t = 0, 0.04, \ldots, 0.4$ (left), and for $t = 0, 0.4, \ldots, 6.4$ (right). Parameters are $N_f = 2048$, $N_c = K_\Gamma^0 = 128$, and $\tau = 2.5 \times 10^{-4}$.

where $\rho := (\mathcal{D}\, c_{\text{sat}})/(R\, c_{\text{solid}}\, v_{\text{kin}})$ and $\alpha := \delta/R$. Since $c_{\text{sat}} \ll c_{\text{solid}}$, we simplify the first equation to

$$\Delta\, u = 0 \quad \text{in} \quad \Omega_+(t). \tag{8}$$

We choose γ and β of order 1, and hence it is important to specify the order of magnitude of the quantities ρ and α in Eq. (7). Taking the values of $c_{\text{sat}}/c_{\text{solid}}$ and v_{kin} from the table in [2, p. 866] into account, we observe that

$$\frac{c_{\text{sat}}}{c_{\text{solid}}\, v_{\text{kin}}} \approx 0.71 \times 10^{-8}\, \text{s}\, (\mu\text{m})^{-1}$$

independently of the temperature T. Moreover, for the time scale $\tilde{t}$, which depends on c_{sat} and hence on T, we obtain a range from 100 s at $-1\,^\circ$C to 1300 s at $-30\,^\circ$C. These time scales seem to be realistic when comparing with the experiments reported in Refs. [2,39].

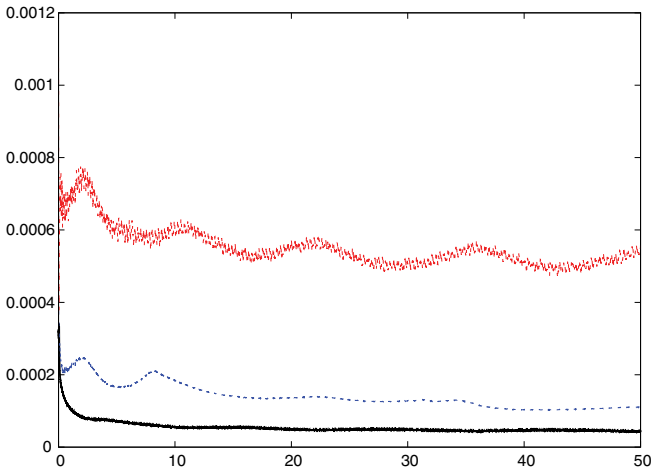

FIG. 9. (Color online) [$\Omega = (-8,8)^2$, $u_{\partial\Omega} = 0.04$, $\gamma = \gamma_{\text{hex}}$, $\beta = 1$] Approximations of $\rho\, \widehat{\mathcal{V}}$ (black, solid), $\alpha\, \kappa_\gamma^{\text{avg}}$ (blue, dashed), and $\alpha\, \kappa_\gamma^{\max}$ (red, dashed) plotted over the time interval [0,50]. Here ρ and α are as in Eq. (9).

For the diffusion constant of water vapor in air we take $\mathcal{D} = 2 \times 10^7\, (\mu\text{m})^2\, \text{s}^{-1}$ (see [2, p. 866]), which is valid at a pressure of 1 atm. With the values of δ and R mentioned above we obtain

$$\rho \approx 1.42 \times 10^{-3}, \quad \alpha = \delta/R \approx 10^{-5}\,. \tag{9}$$

If not otherwise stated, we always choose these parameters in all the numerical computations described in Sec. IV. For the boundary condition we set, recalling Eqs. (3) and (5),

$$u = u_{\partial\Omega} := \frac{c_{\text{super}}}{c_{\text{sat}}} \quad \text{on} \quad \partial\Omega\,. \tag{10}$$

With the help of the table in Ref. [2, p. 866] we compute several exemplary values for the fraction in Eq. (10) for different values of the temperature T and the supersaturation ϱ_{super}; see Table I. In effect, we appear to have reduced the two-parameter variation of the diagram in Fig. 1 to the single parameter $u_{\partial\Omega}$ in Eq. (10). However, in our numerical simulations of snow crystal growth we vary both $u_{\partial\Omega}$ and the kinetic coefficient β. Although in reality not much is known about the possible shapes and dependencies of β, it is known that β strongly depends on T. Thus varying β in our numerical computations may be interpreted as simulating different (yet unknown) temperature regimes.

III. NUMERICAL METHOD AND ANISOTROPIES

For the numerical results in this paper we employ the finite-element approximation introduced by the authors in Refs. [14,40] in order to approximate solutions of Eqs. (6)–(8), and (10). In the method a uniform time step $\tau > 0$ is employed and the evolution of the crystal surface is tracked with the help of parametric meshes Γ^h that are independent from the bulk meshes $\mathcal{T}^h$ on which the approximation u^h of u is computed. The scheme uses an adaptive bulk mesh that has a fine mesh size h_f around Γ^h and a coarse mesh size h_c further away from it. Here $h_f = \frac{2H}{N_f}$ and $h_c = \frac{2H}{N_c}$ are given by two integer numbers $N_f > N_c$, where we assume from now on that

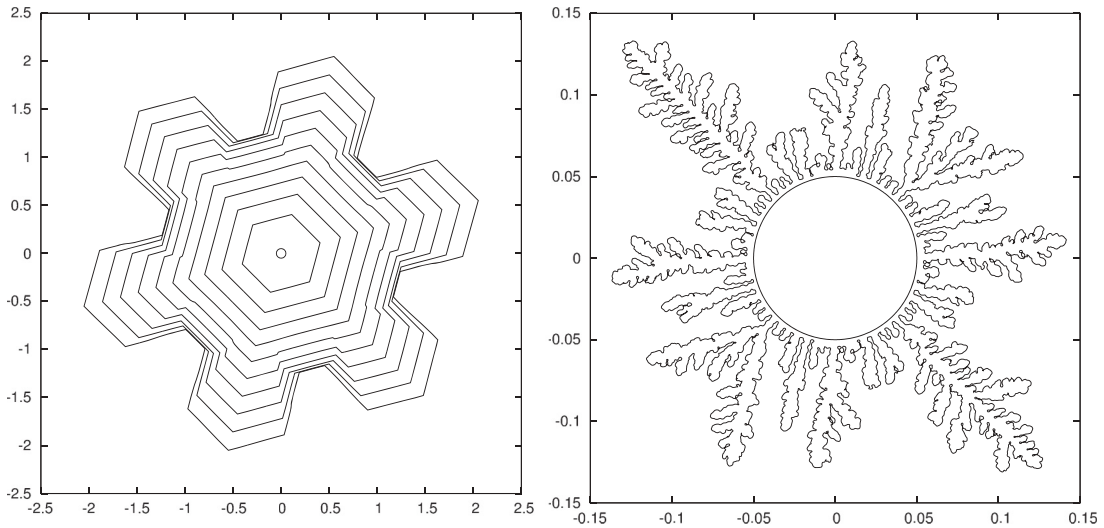

FIG. 10. [$\Omega = (-4,4)^2$, $u_{\partial\Omega} = 0.004$]. We choose $\gamma = \gamma_{\text{hex}}$, $\rho = 0$ with parameters $N_f = 256$, $N_c = 4$, $K_\Gamma^0 = 16$, and $\tau = 0.1$ and plot $\Gamma^h(t)$ for $t = 0{,}50, \ldots, 500$ on the left, and we choose $\alpha = 0$, $\beta = \gamma_{\text{hex}}$ with parameters $N_f = 2048$, $N_c = 128$, $K_\Gamma^0 = 1024$, and $\tau = 10^{-3}$ and plot $\Gamma^h(t)$ for $t = 0$, 3 on the right.

$\Omega = (-H,H)^d$. The initial parametric mesh $\Gamma^h(0)$ consists of K_Γ^0 vertices, and this mesh is locally refined, where elements become too large during the evolution.

In order to successfully model the evolution of anisotropic interface evolution laws the authors introduced a stable discretization in Refs. [14,30]. We now discuss how γ and β have to be chosen in order to model situations with a hexagonal anisotropy. In this paper, we choose surface anisotropies of the form

$$\gamma(\vec{p}) = \sum_{\ell=1}^{L} \gamma_\ell(\vec{p}), \quad \gamma_\ell(\vec{p}) := [\vec{p} \cdot G_\ell \, \vec{p}]^{\frac{1}{2}}, \tag{11}$$

where $G_\ell \in \mathbb{R}^{d\times d}$, for $\ell = 1 \to L$, are symmetric and positive definite matrices, and $\vec{p} = (p_1, \ldots, p_d)^T \in \mathbb{R}^d$ denotes a vector in $\mathbb{R}^d$. We remark that anisotropies of the form (11) admit a formulation of κ_γ in Eq. (7), which can be discretized in a simple and stable way; see [14,30]. We now demonstrate that these forms of γ also allow one to model a hexagonal surface energy in a simple way. To this end, let $l_\epsilon(\vec{p}) := [\epsilon^2 |\vec{p}|^2 + p_1^2 (1-\epsilon^2)]^{\frac{1}{2}} = [p_1^2 + \epsilon^2 \sum_{i=2}^d p_i^2]^{\frac{1}{2}}$ for $\epsilon > 0$.

Then a hexagonal anisotropy in $\mathbb{R}^2$ can be modeled with the choice

$$\gamma(\vec{p}) = \gamma_{\text{hex}}(\vec{p}) := \sum_{\ell=1}^{3} l_\epsilon\left[R\left(\theta_0 + \ell\,\frac{\pi}{3}\right)\vec{p}\right], \tag{12}$$

where $R(\theta) = \left(\begin{smallmatrix} \cos\theta & \sin\theta \\ -\sin\theta & \cos\theta \end{smallmatrix}\right)$ denotes a clockwise rotation through the angle θ and $\theta_0 \in [0, \frac{\pi}{3})$ is a parameter that rotates the orientation of the anisotropy in the plane. The Wulff shape of Eq. (12) for $\epsilon = 0.01$ and $\theta_0 = 0$ is shown in Fig. 2, together

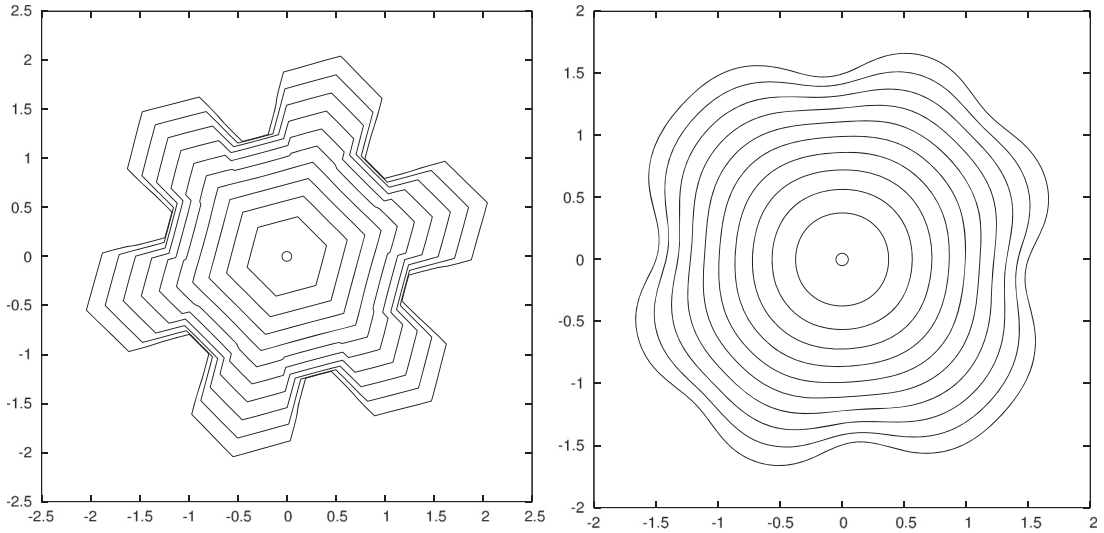

FIG. 11. [$\Omega = (-4,4)^2$, $u_{\partial\Omega} = 0.004$]. We take $\gamma = \gamma_{\text{hex}}$, $\beta = 1$, $N_f = 256$, $N_c = 4$, $K_\Gamma^0 = 16$, and $\tau = 0.1$ on the left and plot $\Gamma^h(t)$ for $t = 0, 50, \ldots, 500$. We take $\gamma = \gamma_{\text{iso}}$, $\beta = \gamma_{\text{hex}}$, $N_f = 512$, $N_c = 16$, $K_\Gamma^0 = 16$, and $\tau = 10^{-2}$ on the right and plot $\Gamma^h(t)$ for $t = 0, 50, \ldots, 500$.

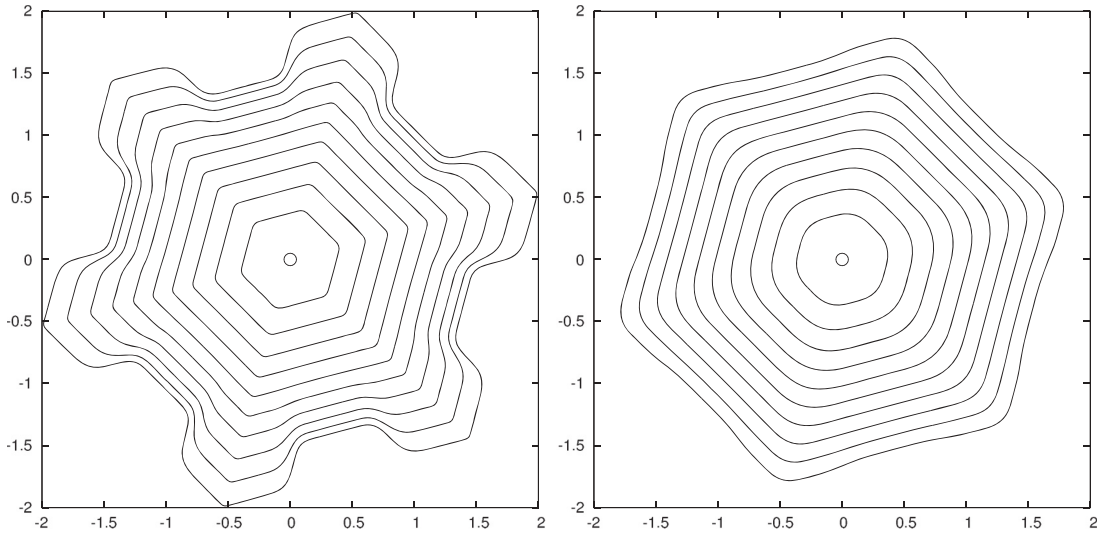

FIG. 12. $[\Omega = (-4,4)^2, u_{\partial\Omega} = 0.004, \gamma$ as in Eq. (15) with $\sigma = 1$ (left) and $\sigma = 5$ (right), $\beta = \gamma_{\rm hex}]\ \Gamma^h(t)$ for $t = 0, 50, \ldots, 500$. Parameters are $N_f = 256$, $N_c = 4$, $K_\Gamma^0 = 16$, and $\tau = 0.1$.

with its polar plot $\mathcal{P} := \{\gamma(\vec{p})\,\vec{p} : |\vec{p}| = 1\}$. For more details on Wulff shapes and polar plots we refer to [38,41].

In order to define anisotropies of the form (11) in $\mathbb{R}^3$, we introduce the rotation matrices $R_1(\theta) := \left(\begin{smallmatrix} \cos\theta & \sin\theta & 0 \\ -\sin\theta & \cos\theta & 0 \\ 0 & 0 & 1 \end{smallmatrix}\right)$ and $R_2(\theta) := \left(\begin{smallmatrix} \cos\theta & 0 & \sin\theta \\ 0 & 1 & 0 \\ -\sin\theta & 0 & \cos\theta \end{smallmatrix}\right)$. In this paper, we consider

$$\gamma(\vec{p}) = \gamma_{\rm hex}(\vec{p}) := l_\epsilon\left[R_2\left(\frac{\pi}{2}\right)\vec{p}\right] + \frac{1}{\sqrt{3}}\sum_{\ell=1}^{3} l_\epsilon\left[R_1\left(\theta_0 + \ell\,\frac{\pi}{3}\right)\vec{p}\right], \qquad (13)$$

which is relevant for the simulation of snow crystal growth. Its Wulff shape for $\epsilon = 0.01$ is shown in Fig. 3, together with its polar plot.

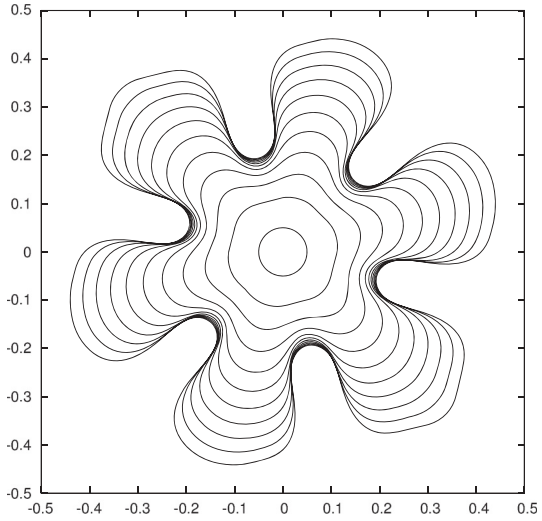

FIG. 13. $[\Omega = (-4,4)^2, u_{\partial\Omega} = 0.04, \gamma = \gamma_{\rm iso}, \beta = \beta_{{\rm hex},L}]\ \Gamma^h(t)$ for $t = 0, 0.5, \ldots, 5$. Parameters are $N_f = 2048$, $N_c = K_\Gamma^0 = 256$, and $\tau = 10^{-3}$.

We note that the Wulff shape of Eq. (13) for $\epsilon \to 0$ approaches a prism, where every face has the same distance from the origin. In other words, for Eq. (13) the surface energy densities in the basal and prismal directions are the same. We remark that if $\mathcal{W}_0$ denotes the Wulff shape of Eq. (13) with $\epsilon = 0$, then the authors in Ref. [23] used the scaled Wulff shape $\frac{1}{2}\,\mathcal{W}_0$ as the building block in their cellular automata algorithm. In addition, we observe that the choice (13) agrees well with data reported, for example, in Ref. [42, p. 148], although there the ratio of basal to prismal energy is computed as $\gamma^{\rm B}/\gamma^{\rm P} \approx 0.92 < 1$. In order to be able to model this situation as well, we generalize the choice (13) to

$$\gamma(\vec{p}) = \gamma_{\rm hex}^{\rm TB}(\vec{p}) := \gamma_{\rm TB}\, l_\epsilon\left[R_2\left(\frac{\pi}{2}\right)\vec{p}\right] + \frac{1}{\sqrt{3}}\sum_{\ell=1}^{3} l_\epsilon\left[R_1\left(\theta_0 + \ell\,\frac{\pi}{3}\right)\vec{p}\right], \qquad (14)$$

so that now $\gamma^{\rm B}/\gamma^{\rm P} = \gamma_{\rm TB}$.

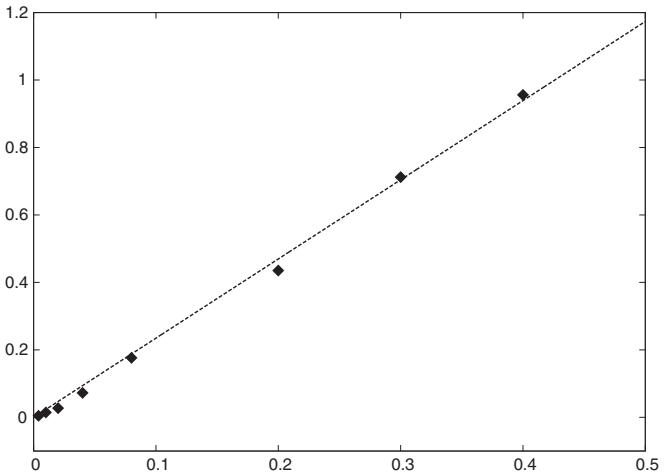

FIG. 14. $[\Omega = (-4,4)^2, \gamma = \gamma_{\rm hex}, \beta = 1]$. Best linear fit for the tip velocity $\widehat{\mathcal{V}}$ against the supersaturation $u_{\partial\Omega}$.

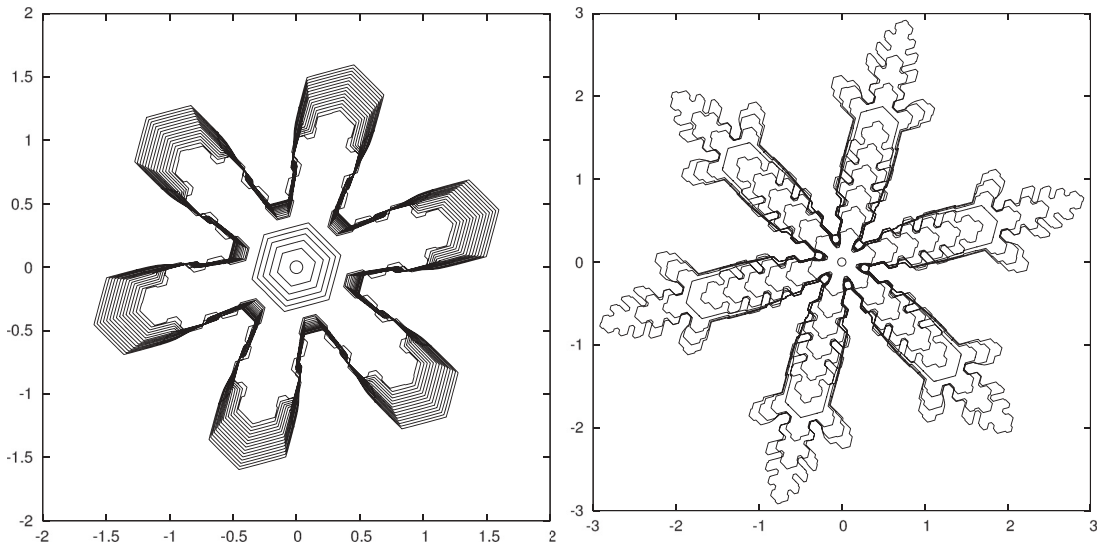

FIG. 15. [$\Omega = (-4,4)^2$, $\gamma = \beta = \gamma_{\text{hex}}$] $\Gamma^h(t)$ for $t = 0,10,\ldots,200$ [left, (19)] and for $t = 0,2,\ldots,12,50,52,54,56$ [right, (20)]. Parameters are $N_f = 1024$, $N_c = K_\Gamma^0 = 64$, and $\tau = 10^{-3}$.

A more generalized form of Eqs. (12) and (13), which also fits into the framework (11), is given by

$$\gamma(\vec{p}) = \gamma_{\text{hex}}(\vec{p}) + \sigma\,|\vec{p}|, \tag{15}$$

where $\sigma \geqslant 0$ is a fixed parameter. For the case $d = 2$ we show scaled Wulff shapes of Eq. (15) for $\sigma = 1$ and $\sigma = 5$ in Fig. 4. We note that for Eq. (15) with $\epsilon = 0$ and $\sigma > 0$, both in the case $d = 2$ and in the case $d = 3$, the corresponding Wulff shape still has flat parts but is now smooth with no corners and, if $d = 3$, with no edges. Equilibrium crystal shapes with these characteristics can be found in certain metals [43], and it is conjectured that they may be relevant for snow crystals as well [44].

As discussed in Ref. [2], and the references therein, the precise values of β as a function of the normal $\vec{\nu}$ are not known. Hence one issue in our computations is to understand how different choices of β influence the overall evolution. First choices for the anisotropy in the kinetic coefficient are $\beta(\vec{\nu}) \equiv 1$ and $\beta = \gamma$. It was discussed in Ref. [2] that the value of β is expected to change with temperature and can vary quite drastically as a function of the orientation. Denoting by β^{B} the condensation coefficient of the basal directions and by β^{P} the condensation coefficient in the prismal directions, it is for example expected that the growth of thin plates at $T = -15\,^\circ\text{C}$ is only possible if $\beta^{\text{P}}/\beta^{\text{B}}$ is large.

In order to be able to vary the kinetic coefficient β significantly, in the case $d = 3$ we define for later use

$$\beta_{\text{flat}}(\vec{p}) = \beta_{\text{flat},\ell}(\vec{p}) := \left[p_1^2 + p_2^2 + 10^{-2\ell}\,p_3^2\right]^{\frac{1}{2}} \tag{16}$$

and

$$\beta_{\text{tall}}(\vec{p}) = \beta_{\text{tall},\ell}(\vec{p}) := \left[10^{-2\ell}\left(p_1^2 + p_2^2\right) + p_3^2\right]^{\frac{1}{2}} \tag{17}$$

with $\ell \in \mathbb{N}$. We note that in practice there is hardly any difference between the numerical results for a kinetic coefficient β that is isotropic in the x_1-x_2 plane, such as β_{flat} and β_{tall}, and one that is anisotropically aligned to the surface energy density, such as $\beta = \beta_{\text{flat}}\,\gamma$. Hence in all our three-dimensional numerical simulations we always choose coefficients β that are isotropic in the x_1-x_2 plane, for example, Eqs. (16) or (17).

In addition, it might be the case that the condensation coefficient β is considerably lower in the directions normal to the facets. In order to model this we choose

$$\begin{aligned}\beta_{\text{hex},L}(\vec{p}) = (&\beta_{\max}\,[\gamma_{\text{hex}}(\vec{p}) - \gamma_{\min}] \\ &+ \beta_{\min}\,[\gamma_{\max} - \gamma_{\text{hex}}(\vec{p})])/(\gamma_{\max} - \gamma_{\min}),\end{aligned} \tag{18}$$

where we fix $\beta_{\max} = 10^3$ and $\beta_{\min} = 1$, and where

$$\begin{aligned}\gamma_{\max} &:= \max_{|\vec{p}|=1} \gamma_{\text{hex}}(\vec{p}) \in \mathbb{R}_{\geqslant 0}, \\ \gamma_{\min} &:= \min_{|\vec{p}|=1} \gamma_{\text{hex}}(\vec{p}) \in \mathbb{R}_{\geqslant 0}.\end{aligned}$$

We note that for the two-dimensional anisotropy (12) it holds that $\gamma_{\max} = \gamma_{\text{hex}}(e^{-i\,\theta_0})$ and $\gamma_{\min} = \gamma_{\text{hex}}(e^{i\,(\frac{\pi}{6} - \theta_0)})$. For more details on the numerical method and the anisotropies we refer readers to [14,29,30,40].

IV. NUMERICAL COMPUTATIONS

A. Snow crystal simulations in two spacial dimensions

In all computations for Eqs. (6)–(8), and (10) in this subsection, if not otherwise stated, we use the parameters (9) and choose the surface energy anisotropy $\gamma = \gamma_{\text{hex}}$ defined by (12) with $\epsilon = 0.01$ and $\theta_0 = \frac{\pi}{12}$. The rotation in the definition of the anisotropy is used, so that the dominant growth directions are not exactly aligned with the underlying bulk meshes $\mathcal{T}^h$. Moreover, the radius of the circular initial crystal seed, $\Gamma(0)$, is always chosen to be 0.05.

First of all we study what influences the curvature and the velocity terms in Eq. (7) and the supersaturation in Eq. (10) have on the evolution of the crystal. We choose the supersaturation $u_{\partial\Omega} = 0.004$ and show the results in Fig. 5. One observes that the hexagonal structure of the crystal forms quickly and that the facets become unstable and break after they reached a certain size—a phenomenon which is observed in experiments as well; see [2].

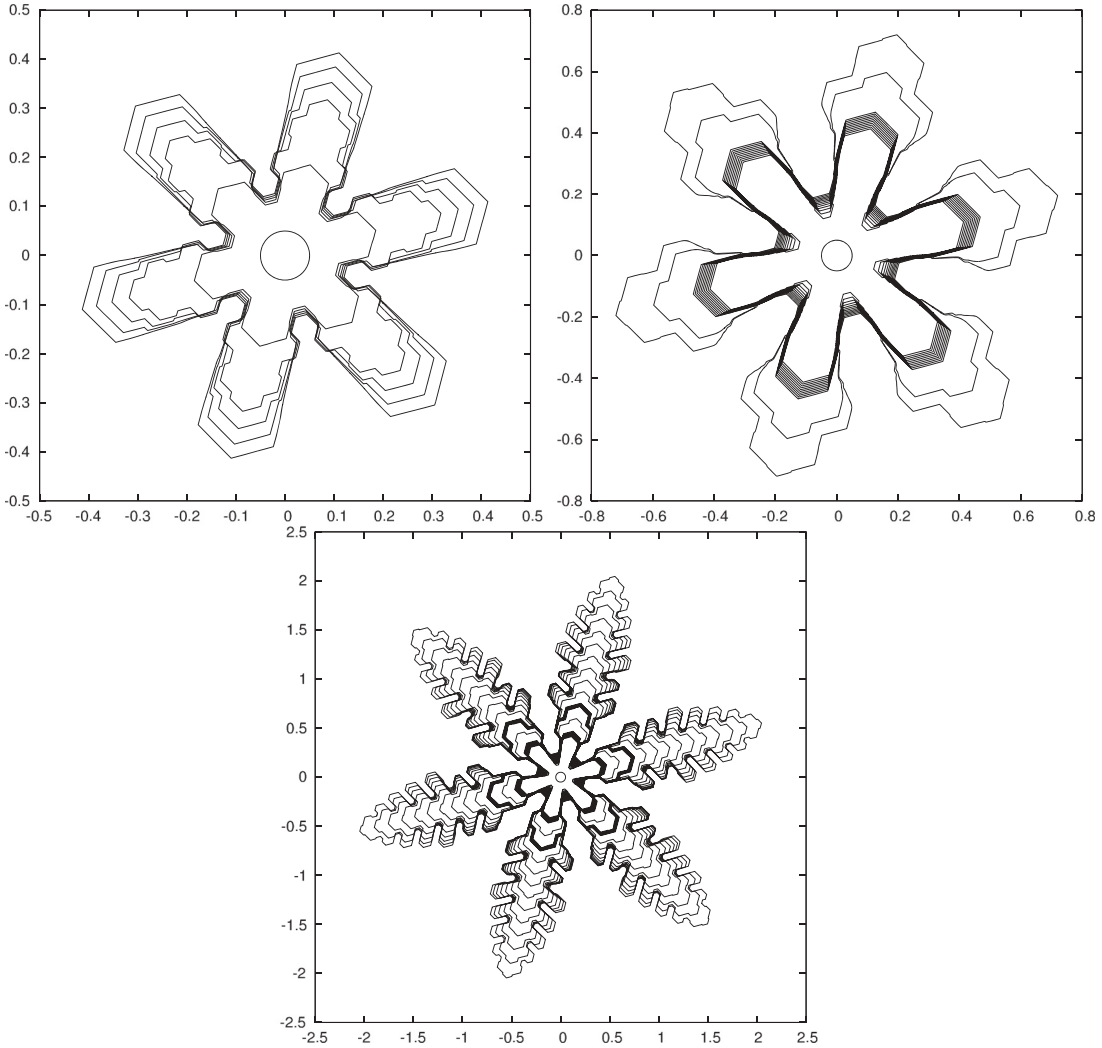

FIG. 16. $[\Omega = (-4,4)^2,\ \gamma = \beta = \gamma_{\text{hex}}]\ \Gamma^h(t)$ for $t = 0,0.2,\ldots,1$ (left top), $t = 0,1,\ldots,12$ (right top), and $t = 0,1,\ldots,30$ (bottom). Parameters are $N_f = 2048$, $N_c = K_\Gamma^0 = 128$, and $\tau = 2.5 \times 10^{-4}$.

In Figures 6–8 we plot computations with larger supersaturations, $u_{\partial\Omega} = 0.01,0.04,0.2$. One clearly observes dendritic growth, which is more enhanced at larger supersaturations. In addition, the evolution is much faster due to the fact that more water vapor molecules are available.

It is also of interest to compare the size of the terms appearing in Eq. (7). To this end, we compare the numerical approximations of the terms

$$\rho\,\widehat{\mathcal{V}}, \quad \alpha\,\kappa_\gamma^{\text{avg}}, \quad \alpha\,\kappa_\gamma^{\max}$$

where $\widehat{\mathcal{V}}$ denotes the observed tip velocity (i.e., the velocity of the part of the interface furthest away from the origin), $\kappa_\gamma^{\text{avg}}$ is the average of $|\kappa_\gamma|$ on the interface, and $\kappa_\gamma^{\max}$ is the maximum of $|\kappa_\gamma|$. For a computation with $\gamma = \gamma_{\text{hex}}$, $\beta = 1$, and $u_{\partial\Omega} = 0.04$ we plot these values in Fig. 9. It clearly can be seen that the curvature contribution is larger than the velocity term. In our other computations we observed only for supersaturations around 0.2 and larger that the velocity term $\rho\,\widehat{\mathcal{V}}$ is larger than the average curvature term $\alpha\,\kappa_\gamma^{\text{avg}}$.

In Fig. 10 we set the velocity term to zero in the left computation, $\rho = 0$, and we set the curvature term to zero in the right computation, $\alpha = 0$. We observe that leaving out the velocity term only has a very minor impact on the crystal evolution. On the other hand, leaving out the curvature term has a drastic effect: The front becomes very unstable. This can be explained as follows. Growth from supersaturated vapor is unstable and while the velocity term in Eq. (7) without the curvature term can dampen the unstable modes, they are still unstable on all wavelengths. The curvature term, on the other hand, will stabilize the small wavelengths and will select a fastest growing wavelength, irrespective of the velocity term.

We now study the influence of the anisotropy on the evolution. On the left of Fig. 11 we present an evolution with a hexagonal anisotropy for γ and an isotropic β. In the same figure on the right we take γ as isotropic and β as hexagonal. One clearly observes that anisotropy in the surface energy seems to be important to obtain faceted growth.

This is underlined by the next computation, where we choose Eq. (15) for the anisotropy γ, and let $\beta = \gamma_{\text{hex}}$. In Fig. 12 we present evolutions for $\sigma = 1$ and $\sigma = 5$. These computations show how important the faceted anisotropy in the Wulff shape is in order to obtain faceted snow crystals; recall Fig. 4.

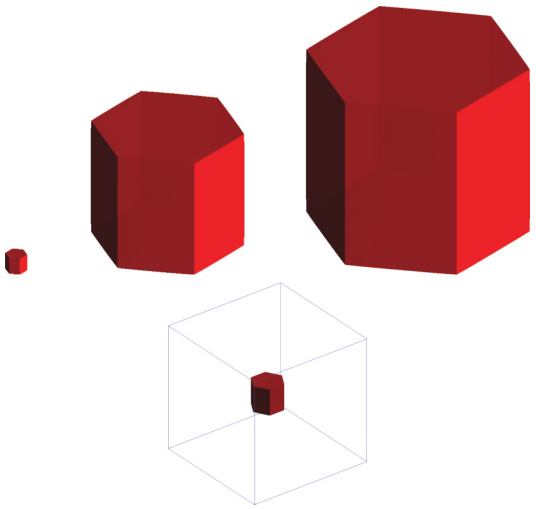

FIG. 17. (Color online) $[\Omega = (-8,8)^3,\ \gamma = \beta = \gamma_{\text{hex}}^{\text{TB}}$ with $\gamma_{\text{TB}} = 0.95]$ $\Gamma^h(t)$ for $t = 0, 0.1, 0.2$; and $\Gamma^h(0.2)$ within Ω. Parameters are $N_f = 512$, $N_c = 32$, $K_\Gamma^0 = 1538$, and $\tau = 10^{-4}$.

It was suggested by Prof. Libbrecht [44] that the difference of β as a function of $\vec{\nu}$ might be large with a minimum in the the directions of the facet normals. We hence take $\beta = \beta_{\text{hex},L}$ and $\gamma = \gamma_{\text{iso}}$ in Fig. 13. One observes that the anisotropy in the condensation coefficient β is large enough to lead to a sixfold branching structure, but it is also clear that the anisotropy in β does not lead to faceted growth.

Next we study how the tip velocity in a growing dendritic crystal depends on the supersaturation. So far nothing is known theoretically for this dependence in the case of faceted growth (see [2, §4]), even though for simpler problems (i.e., in the absence of faceting) a vast literature exists; see [38] and the references therein. As can be seen in Fig. 9, the tip velocity after some time becomes basically time independent. This is true also for our other computations with different supersaturations. We observe a linear dependence between the supersaturation and the tip velocity that the evolution eventually settles on. To underline this qualitative behavior, we numerically determine the value for the nearly constant tip velocity $\widehat{\mathcal{V}}$ for several values of $u_{\partial\Omega}$; see Fig. 14 for a plot of these velocities. We also show the best linear fit to this data, which is given by a linear function with slope $\approx$2.35. We remark that a similar linear relationship between velocity and supersaturation has been observed experimentally for needles; see [34].

We end this subsection with some computations, where we use a time-dependent choice for $u_{\partial\Omega}$. This models changing

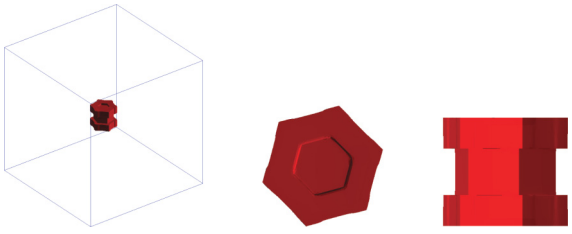

FIG. 18. (Color online) $[\Omega = (-4,4)^3,\ u_{\partial\Omega} = 0.004,\ \gamma = \gamma_{\text{hex}},\ \beta = 1]$ $\Gamma^h(50)$. Parameters are $N_f = 128$, $N_c = 16$, $K_\Gamma^0 = 98$, and $\tau = 10^{-1}$.

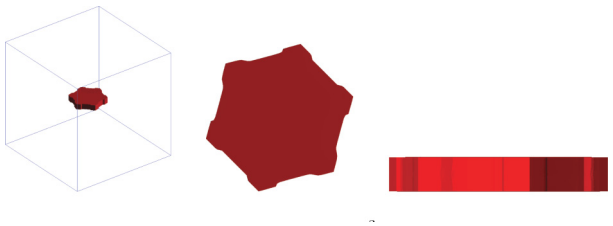

FIG. 19. (Color online) $[\Omega = (-4,4)^3,\ u_{\partial\Omega} = 0.004,\ \gamma = \gamma_{\text{hex}},\ \beta = \beta_{\text{flat},2}]$ $\Gamma^h(50)$. Parameters are $N_f = 128$, $N_c = 16$, $K_\Gamma^0 = 98$, and $\tau = 10^{-1}$.

physical conditions. In particular, in the first computation we set

$$u_{\partial\Omega}(t) = \begin{cases} 0.004 & t \in [0,50) \cup [60,200], \\ 0.08 & t \in [50,60); \end{cases} \tag{19}$$

while in the second computation we set

$$u_{\partial\Omega}(t) = \begin{cases} 0.08 & t \in [0,12) \cup [50,56], \\ 0.004 & t \in [12,50); \end{cases} \tag{20}$$

see Fig. 15 for the results. In the last computation we use a widely varying $u_{\partial\Omega}$. We set $u_{\partial\Omega}(t) = 0.2$ for $t \in [0,0.2)$, then $u_{\partial\Omega}(t) = 0.4$ until $t = 0.3$, then $u_{\partial\Omega}(t) = 0.08$ until $t = 1$, then $u_{\partial\Omega}(t) = 0.004$ until $t = 10$, then $u_{\partial\Omega}(t) = 0.08$ until $t = 12$, then $u_{\partial\Omega}(t) = 0.004$ until $t = 20$, and then $u_{\partial\Omega}(t) = 0.08$ until the end; see Fig. 16 for the results.

B. Snow crystal simulations in three spacial dimensions

Also in three spacial dimensions we use the physically relevant parameters introduced in Sec. II, see in particular Eq. (9), and choose, if not stated otherwise, the three-dimensional variant of γ_{hex}, see Eq. (13), with $\epsilon = 0.01$ and $\theta_0 = \frac{\pi}{12}$. In all computations with the exception of Fig. 17 the initial crystal seed was spherical with radius 0.05. Similarly to our computations in two spacial dimensions, we observe in our three-dimensional numerical computations that the surface energy anisotropy is important in order to obtain faceted growth. If we do not choose the surface energy strongly faceted, then we do not observe faceted growth of the crystal.

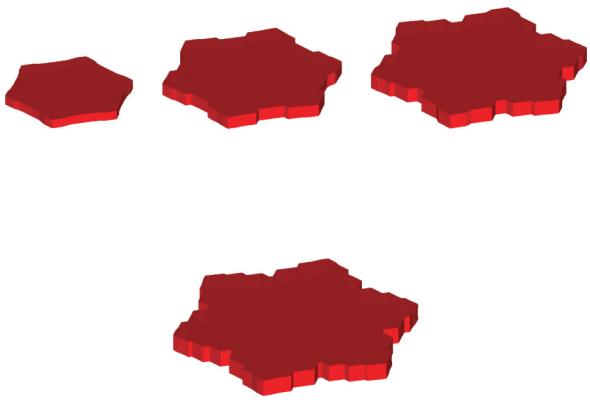

FIG. 20. (Color online) $[\Omega = (-8,8)^3,\ u_{\partial\Omega} = 0.004,\ \gamma = \gamma_{\text{hex}},\ \beta = \beta_{\text{flat},3}]$ $\Gamma^h(t)$ for $t = 50, 100, 150, 200$. Parameters are $N_f = 256$, $N_c = 32$, $K_\Gamma^0 = 98$, and $\tau = 10^{-1}$.

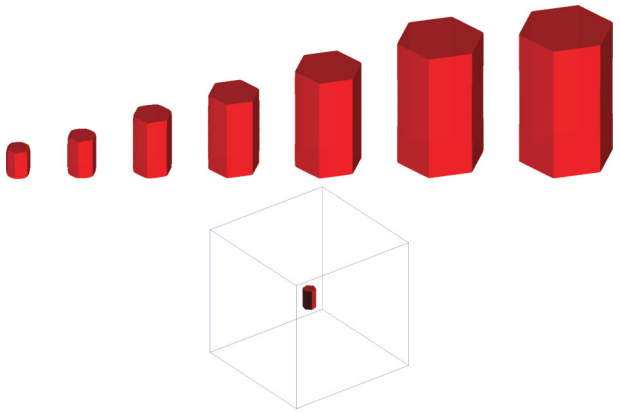

FIG. 21. (Color online) $[\Omega = (-4,4)^3$, $u_{\partial\Omega} = 0.002$, $\gamma = \gamma_{\text{hex}}$, $\beta = \beta_{\text{tall},1}]$ $\Gamma^h(t)$ for $t = 1, 2, 5, 10, 20, 40, 50$; and $\Gamma^h(50)$ within Ω. Parameters are $N_f = 128$, $N_c = 16$, $K_\Gamma^0 = 98$, and $\tau = 10^{-1}$.

One issue in three dimensions is to understand how the parameter β leads to either horizontal flat growth or to columnar vertical growth, which may yield solid prisms or needles, respectively. First of all, we attempt to compute a self-similar hexagonal evolution, that is, a crystal where the basal and prismal facets grow with the same velocity. This is motivated by a theoretical result in Ref. [45], in which the existence of self-similar evolutions of crystals, where the Wulff shape is a cylinder, was shown. We choose $\rho = \alpha = 1$, $u_{\partial\Omega} = 21$, $\gamma = \beta = \gamma_{\text{hex}}^{\text{TB}}$ as in Eq. (14), vary the ratio $\gamma_{\text{TB}} = \gamma^{\text{B}}/\gamma^{\text{P}}$, and observe that, upon starting the evolution with $\Gamma(0)$ being a scaled Wulff shape, for $\gamma_{\text{TB}} \approx 0.95$ the evolution is self-similar up to discretization errors. See Fig. 17 for a computation with $\gamma_{\text{TB}} = 0.95$.

For the remainder of the computations we fix $\gamma_{\text{TB}} = 1$; that is, we choose $\gamma = \gamma_{\text{hex}}$ as in Eq. (13), and use the physically relevant parameters in Eq. (9). For the first such computation we set $u_{\partial\Omega} = 0.004$ and $\beta = 1$; see Fig. 18. We can clearly see that the facets of the growing crystal are aligned with the Wulff shape of γ. We also note that facet breaking occurs in both the prismal and the basal directions. In this context we refer to [39], where similar facet breaking was observed in experiments.

It is well known that the condensation coefficient β varies strongly for different orientations, depending on the meteorological environment. In particular, the value of β can differ quite drastically between directions which correspond to basal facet normals and ones which correspond to prismal facet normals; see [2]. We hence perform different numerical computations for the condensation coefficients β_{flat} and β_{tall} defined in Eqs. (16) and (17).

We begin with a repeat of the simulation in Fig. 18, but now we choose as kinetic coefficient $\beta = \beta_{\text{flat},2}$ and $\beta = \beta_{\text{flat},3}$; see Figs. 19 and 20. In comparison to the evolution in Fig. 18 one observes that the smaller condensation coefficient in basal directions leads to flat crystals. This is related to shapes in the Nakaya diagram for temperatures between $0\,^\circ$C and $-3\,^\circ$C and between $-10\,^\circ$C and $-22\,^\circ$C.

A computation with a supersaturation $u_{\partial\Omega} = 0.002$ and $\beta = \beta_{\text{tall},1}$ can be seen in Fig. 21. In this case the condensation coefficient is larger in the basal direction and we obtain a solid prism, which can be found in the Nakaya diagram at temperatures between $-5\,^\circ$C and $-10\,^\circ$C and at low supersaturations.

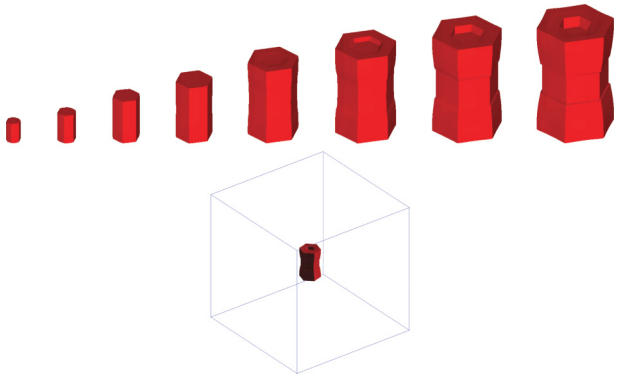

FIG. 22. (Color online) $[\Omega = (-4,4)^3$, $u_{\partial\Omega} = 0.004$, $\gamma = \gamma_{\text{hex}}$, $\beta = \beta_{\text{tall},1}]$ $\Gamma^h(t)$ for $t = 1, 2, 5, 10, 20, 30, 40, 50$; and $\Gamma^h(50)$ within Ω. Parameters are $N_f = 128$, $N_c = 16$, $K_\Gamma^0 = 98$, and $\tau = 10^{-1}$.

At higher supersaturations $u_{\partial\Omega} = 0.004$ we obtain for $\beta = \beta_{\text{tall},1}$ the results shown in Fig. 22. We also give some plots of the rescaled water vapor density in Fig. 23. We observe Berg's effect [46], which states that the concentration is largest at the edges and decreases towards the center of the facet. It is believed that facet breaking occurs when the concentration becomes too nonuniform on the facets [47]. In Fig. 22 we observe facet breaking for the basal and prismal directions, although the breaking predominantly occurs on the basal facets.

Choosing the condensation coefficient even larger in the basal directions leads to Fig. 24. We observe hollow columns as in the Nakaya diagram between $-5\,^\circ$C and $-10\,^\circ$C at low, but not very low, supersaturations. Increasing the condensation coefficient in the basal directions even further (i.e., choosing $\beta = \beta_{\text{tall},3}$) leads to the evolution depicted on the left of Fig. 25. On the right we also display a computation on a coarser grid.

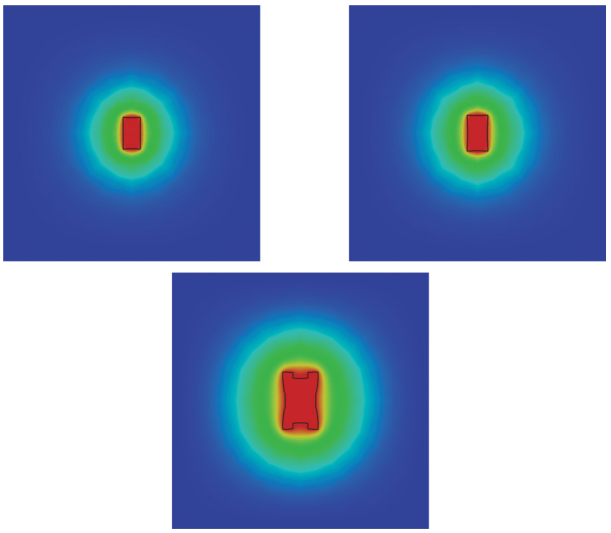

FIG. 23. (Color online) $[\Omega = (-4,4)^3$, $u_{\partial\Omega} = 0.004$, $\gamma = \gamma_{\text{hex}}$, $\beta = \beta_{\text{tall},1}]$ $\Gamma^h(t) \cap \{\vec{x} : x_1 = 0\}$ and $u^h(t)|_{x_1=0}$ for $t = 15, 20, 50$. The colors for u^h vary between red for $u^h = -1.12 \times 10^{-4}$ and blue for $u^h = 4 \times 10^{-3}$. Parameters are $N_f = 128$, $N_c = 16$, $K_\Gamma^0 = 98$, and $\tau = 10^{-1}$.

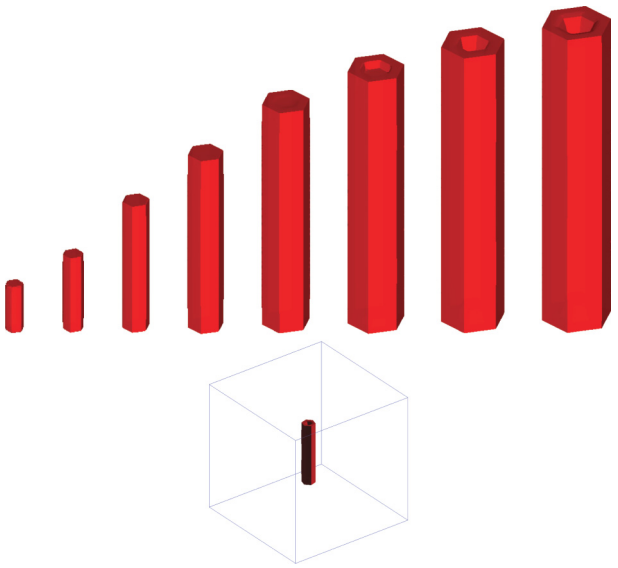

FIG. 24. (Color online) $[\Omega = (-4,4)^3,\ u_{\partial\Omega} = 0.008,\ \gamma = \gamma_{\text{hex}},\ \beta = \beta_{\text{tall},2}]\ \Gamma^h(t)$ for $t = 1, 2, 5, 10, 20, 30, 40, 50$; and $\Gamma^h(50)$ within Ω. Parameters are $N_f = 128$, $N_c = 16$, $K_\Gamma^0 = 98$, and $\tau = 10^{-1}$.

Both results in Fig. 25 lead to needle growth, which also appears in the Nakaya diagram. We remark that the shape on the right of Fig. 25 is caused by numerical noise and rounding errors. However, the same effect, on even the most refined meshes, can be achieved by adding random fluctuations to the model. In real life such fluctuations and changes in physical parameters are experienced by the growing snow crystal, as it moves through the atmosphere toward the earth.

A numerical simulation with supersaturation $u_{\partial\Omega} = 0.02$ with $\beta = \beta_{\text{flat},3}$ is displayed in Fig. 26. In this case capped columns appear, which can also be observed in nature; see [2,48].

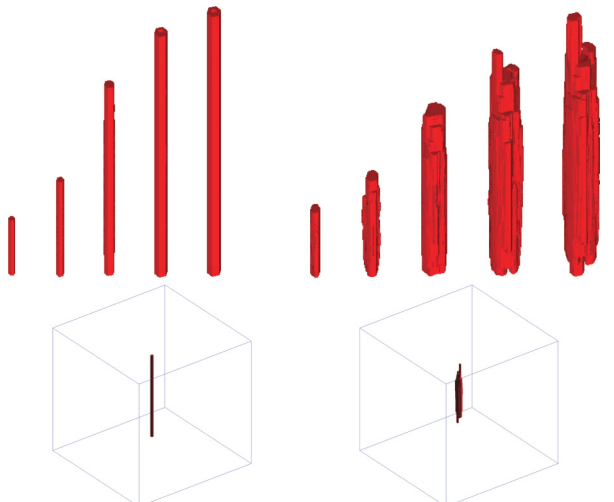

FIG. 25. (Color online) $[\Omega = (-8,8)^3,\ u_{\partial\Omega} = 0.004,\ \gamma = \gamma_{\text{hex}},\ \beta = \beta_{\text{tall},3}]\ \Gamma^h(t)$ for $t = 5, 10, 30, 50, 60$; and $\Gamma^h(60)$ within Ω. Parameters are $N_f = 512$, $N_c = 32$, $K_\Gamma^0 = 98$, and $\tau = 10^{-2}$ (left), and $N_f = 256$, $N_c = 32$, $K_\Gamma^0 = 98$, and $\tau = 10^{-1}$ (right).

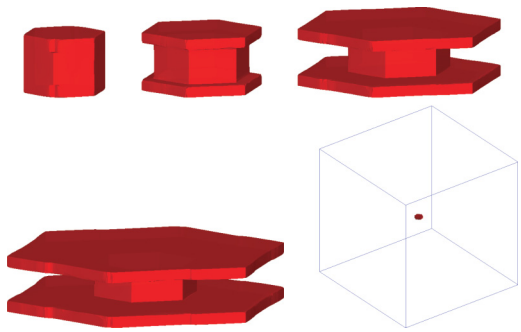

FIG. 26. (Color online) $[\Omega = (-4,4)^3,\ u_{\partial\Omega} = 0.02,\ \gamma = \gamma_{\text{hex}},\ \beta = \beta_{\text{flat},3}]\ \Gamma^h(t)$ for $t = 0.05, 0.1, 0.2, 0.3$; and $\Gamma^h(0.3)$ within Ω. Parameters are $N_f = 512$, $N_c = 32$, $K_\Gamma^0 = 1538$, and $\tau = 5 \times 10^{-4}$.

We end this subsection with computations, where we use a time-dependent choice for $u_{\partial\Omega}$. In particular, we set

$$u_{\partial\Omega}(t) = \begin{cases} 0.004 & t \in [0,15) \cup [18,50], \\ 0.024 & t \in [15,18). \end{cases} \tag{21}$$

See Fig. 27 for the results. First a solid plate forms and then, due to the fact that the supersaturation increases, the plate becomes unstable and new platelike shapes grow at the corners of the plate.

Finally, we perform two simulations, where we vary β in time. In the first such example, we choose

$$\beta(\vec{p}) = \begin{cases} \beta_{\text{flat},3}(\vec{p}) & t \in [0,30), \\ \beta_{\text{tall},3}(\vec{p}) & t \in [30,50]. \end{cases} \tag{22}$$

In a second example, we choose

$$\beta(\vec{p}) = \begin{cases} \beta_{\text{flat},3}(\vec{p}) & t \in [0,20), \\ \beta_{\text{flat},1}(\vec{p}) & t \in [20,50]. \end{cases} \tag{23}$$

Results for these choices of β and for $u_{\partial\Omega} = 0.004$ can be seen in Fig. 28. We observe scrolls on plates, a shape that is also called plates with scrolls at ends, which also appear in the

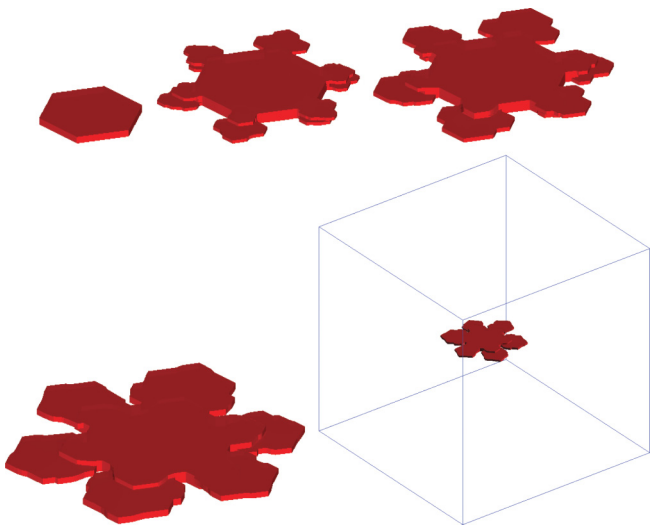

FIG. 27. (Color online) $[\Omega = (-8,8)^3,\ u_{\partial\Omega}$ as in Eq. (21), $\gamma = \gamma_{\text{hex}},\ \beta = \beta_{\text{flat},3}]\ \Gamma^h(t)$ for $t = 15, 20, 30, 50$; and $\Gamma^h(50)$ within Ω. Parameters are $N_f = 512$, $N_c = 32$, $K_\Gamma^0 = 98$, and $\tau = 2 \times 10^{-2}$.

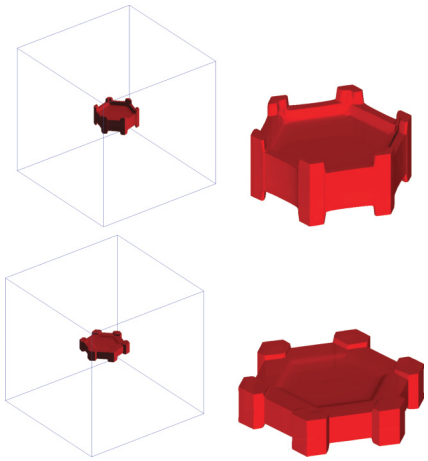

FIG. 28. (Color online) [$\Omega = (-4,4)^3$, $u_{\partial\Omega} = 0.004$, $\gamma = \gamma_{\text{hex}}$, β as in (22) (top), and as in (28) (bottom)] $\Gamma^h(50)$. Parameters are $N_f = 128$, $N_c = 16$, $K_\Gamma^0 = 98$, and $\tau = 10^{-1}$.

Magono-Lee classification of natural snow crystals [49]; see also [42, p. 46] and [48].

V. CONCLUSIONS

We have demonstrated that an approach introduced by the authors in Refs. [14,30,40] provides a powerful computational tool to investigate pattern formation in crystal growth. The method makes it possible to simulate faceted and dendritic growth simultaneously. We also observe the instability of crystals leading to facet breaking. Many parameters in models for crystal growth are not known. The presented numerical method in combination with a comparison to experimental results can make it possible to estimate the relative sizes of parameters. In particular, by varying the condensation coefficient we were able to observe either platelike growth or columnar growth.

Let us summarize the results:

(1) Surface energy effects taking anisotropy into account have been included in the model and, despite their small size, totally change the character of the interfacial dynamics. In our computations an anisotropic surface energy is required to produce faceted dendritic growth.

(2) The influence of the anisotropy in the condensation coefficient, at least at small supersaturations, is not sufficient for faceted growth.

(3) For small supersaturations the influence of the velocity term in Eq. (7) is small in comparison with the curvature term.

(4) The velocity at the tip of growing crystals depends in a linear way on the supersaturation.

(5) Macroscopic models for crystal growth based on a diffusion equation in the gas phase, a mass balance on the vapor crystal interface, and a modified Gibbs–Thomson law, taking attachment kinetics into account, are able to model a variety of phenomena in crystal growth, such as the appearance of solid plates, solid prisms, hollow columns, needles, dendrites, capped columns, and scrolls on plates.

ACKNOWLEDGMENT

The authors express their deep thanks to Prof. K. G. Libbrecht of the California Institute of Technology for many fruitful discussions and for providing Fig. 1.

[1] U. Nakaya, *Snow Crystals: Natural and Artificial* (Cambridge University Press, Cambridge, 1954).
[2] K. G. Libbrecht, Rep. Prog. Phys. **68**, 855 (2005).
[3] http://www.snowcrystals.com.
[4] J. G. Dash, A. W. Rempel, and J. S. Wettlaufer, Rev. Mod. Phys. **78**, 695 (2006).
[5] Y. Furukawa, M. Yamamoto, and T. Kuroda, J. Cryst. Growth **82**, 665 (1987).
[6] M. Elbaum, Phys. Rev. Lett. **67**, 2982 (1991).
[7] M. Elbaum, S. G. Lipson, and J. G. Dash, J. Cryst. Growth **129**, 491 (1993).
[8] G. Sazakia, S. Zepedaa, S. Nakatsubo, M. Yokomine, and Y. Furukawa, Proc. Natl. Acad. Sci. USA **109**, 1052 (2006).
[9] A. R. Roosen and J. E. Taylor, Mater. Res. Soc. Symp. Proc. **237**, 25 (1991).
[10] E. Yokoyama, J. Cryst. Growth **128**, 251 (1993).
[11] E. Yokoyama and R. F. Sekerka, J. Cryst. Growth **125**, 389 (1992).
[12] A. Schmidt, J. Comput. Phys. **195**, 293 (1996).
[13] A. Schmidt, in *Proceedings of the Algoritmy '97 Conference on Scientific Computing (Zuberec)*, edited by J. Kačur and K. Mikula, Vol. 67 (Slovak University of Technology, Bratislava, 1998), pp. 57–68.
[14] J. W. Barrett, H. Garcke, and R. Nürnberg, J. Comput. Phys. **229**, 6270 (2010).
[15] J. A. Sethian and J. Strain, J. Comput. Phys. **98**, 231 (1992).
[16] R. Kobayashi, Physica D **63**, 410 (1993).
[17] A. A. Wheeler, B. T. Murray, and R. J. Schaefer, Phys. D **66**, 243 (1993).
[18] A. Karma and W.-J. Rappel, Phys. Rev. E **57**, 4323 (1998).
[19] J.-M. Debierre, A. Karma, F. Celestini, and R. Guérin, Phys. Rev. E **68**, 041604 (2003).
[20] T. Uehara and R. F. Sekerka, J. Cryst. Growth **254**, 251 (2003).
[21] C. A. Reiter, Chaos, Solitons & Fractals **23**, 1111 (2005).
[22] K. G. Libbrecht, arXiv:0807.2616.
[23] J. Gravner and D. Griffeath, Phys. Rev. E **79**, 011601 (2009).
[24] Y. Furukawa and H. Nada, J. Phys. Chem. B **101**, 6167 (1997).
[25] H. Nada, J. P. van der Eerden, and Y. Furukawa, J. Cryst. Growth **266**, 297 (2004).
[26] H. Nada and Y. Furukawa, J. Cryst. Growth **283**, 242 (2005).
[27] J. W. Barrett, H. Garcke, and R. Nürnberg, J. Comput. Phys. **222**, 441 (2007).
[28] J. W. Barrett, H. Garcke, and R. Nürnberg, J. Comput. Phys. **227**, 4281 (2008).
[29] J. W. Barrett, H. Garcke, and R. Nürnberg, IMA J. Numer. Anal. **28**, 292 (2008).

[30] J. W. Barrett, H. Garcke, and R. Nürnberg, Numer. Math. **109**, 1 (2008).
[31] J. W. Barrett, H. Garcke, and R. Nürnberg, Eur. J. Appl. Math. **21**, 519 (2010).
[32] J. W. Barrett, H. Garcke, and R. Nürnberg (unpublished).
[33] K. G. Libbrecht and M. E. Rickerby, arXiv:1110.5828.
[34] K. G. Libbrecht, T. Crosby, and M. Swanson, J. Cryst. Growth **240**, 241 (2002).
[35] E. Ben-Jacob, Contemp. Phys. **34**, 247 (1993).
[36] J. W. Cahn and D. W. Hoffman, Acta Metall. **22**, 1205 (1974).
[37] J. E. Taylor, J. W. Cahn, and C. A. Handwerker, Acta Metall. Mater. **40**, 1443 (1992).
[38] S. H. Davis, *Theory of Solidification* (Cambridge University Press, Cambridge, 2001).
[39] T. Gonda and T. Yamazaki, J. Cryst. Growth **60**, 259 (1982).
[40] J. W. Barrett, H. Garcke, and R. Nürnberg, arXiv:1201.1802.
[41] M. E. Gurtin, *Thermomechanics of Evolving Phase Boundaries in the Plane* (Clarendon Press, New York, 1993).
[42] H. R. Pruppacher and J. D. Klett, *Microphysics of Clouds and Precipitation* (Kluwer, Dordrecht, the Netherlands, 1997).
[43] H. P. Bonzel, Phys. Rep. **385**, 1 (2003).
[44] K. G. Libbrecht (private communication).
[45] Y. Giga and P. Rybka, Interfaces Free Bound. **6**, 405 (2004).
[46] W. F. Berg, Proc. R. Soc. London A **164**, 79 (1938).
[47] Y. Giga and P. Rybka, Adv. Math. Sci. Appl. **13**, 625 (2003).
[48] K. G. Libbrecht, *Field Guide to Snowflakes* (Voyageur Press, Saint Paul, Minnesota, 2006).
[49] C. Magono and C. W. Lee, J. Fac. Sci., Hokkaido Univ., Ser. VII **2**, 321 (1966), http://hdl.handle.net/2115/8672.